Moving Discretized Control Set Model-Predictive Control for Dual-Active Bridge With the Triple-Phase Shift

Linglin Chen, Lyuyi Lin, Shuai Shao, *Member, IEEE*, Fei Gao, *Member, IEEE*, Zhenyu Wang, *Member, IEEE*, Patrick W. Wheeler, *Senior Member, IEEE*, and Tomislav Dragičević, *Senior Member, IEEE*

***Abstract*—Triple-phase shift (TPS) is commonly utilized to enhance the efficiency of the dual-active-bridge (DAB) converters. However, the small-signal model of the circuit varies with operating mode, terminal voltage ratio, and power. In order to address this issue, a control inspired by the finite-control set model-predictive control is proposed. The proposed moving discretized control set model-predictive control (MDCS-MPC) can achieve great control flexibility and good transition performance throughout the power and terminal voltage range with global control parameters. It presents fixed switching frequency with low computational burden due to the utilization of only two prediction horizons. The operating principle of the proposed MDCS-MPC is introduced in development of a cost function that provides stiff load voltage regulation. The steady-state error in MDCS-MPC has also been analyzed and compensated. The application of MDCS-MPC in a multiobjective control scenario has been addressed. Experiments on a 300-V/300-V 20-kHz 1-kW DAB converter are carried out to verify the theoretical claims.**

***Index Terms*—Dual-active bridge (DAB), model-predictive control (MPC).**

NOMENCLATURE

f_s	Switching frequency.
T_s	Time in one switching period.
r_V	Terminal voltage ratio.
V_{HV1}	Primary dc terminal voltage.
V_{HV2}	Secondary dc terminal voltage.
$v_{\rm ac1}$	Primary transformer port voltage.
$v_{\rm ac2}$	Secondary transformer port voltage.
D_1	Duty cycle of $v_{\rm ac1}$.
D_2	Duty cycle of $v_{\rm ac2}$.
D_f	Phase shift between $v_{\rm ac1}$ and $v_{\rm ac2}$.
L_p	Power transferring inductance on primary side.
L_m	Transformer magnetizing inductance.
C_{HV1}	DC capacitor on primary side.
C_{VH2}	DC capacitor on secondary side.
i_c	Current flowing into C_{HV2}.
$i_{\rm ac2}$	Transformer secondary current.
i_{HV1}	Primary H-bridge dc-side current.
i_{HV2}	Secondary H-bridge dc-side current.
$I_{\rm load}$	Load current.
μ	Points to be calculated in T_s.
μ_m	Maximum number of discretized elements.
V_{HV2_ref}	Reference dc bus voltage.
Δ_f	Finest step achievable by the digital control platform.
$\Delta_{\rm adp}$	The adaptive step.
G_1, G_2	Cost function terms.
α_1, α_2	Weighting factors.
$I_{\rm comp\_f}$	Prediction error compensation term.

Manuscript received July 5, 2019; revised November 9, 2019; accepted December 25, 2019. Date of publication December 29, 2019; date of current version April 22, 2020. This work was supported by the Office of Naval Research Global under the Award N62909-17-1-2106. Recommended for publication by Associate Editor C. Fernandez. *(Corresponding authors: Shuai Shao; Fei Gao.)*

L. Chen, Z. Wang, and P. W. Wheeler are with the Department of Electrical and Electronics Engineering, University of Nottingham, Nottingham NG7 2RD, U.K. (e-mail: timzjuuon@gmail.com; zhenyu.wang@nottingham.ac.uk; pat.wheeler@nottingham.ac.uk).

L. Lin and S. Shao are with the College of Electrical Engineering, Zhejiang University, Hangzhou 310027, China (e-mail: lin61@zju.edu.cn; shaos@zju.edu.cn).

F. Gao is with the Department of Electrical Engineering, Shanghai Jiao Tong University, Shanghai 200240, China (e-mail: fei.gao@sjtu.edu.cn).

T. Dragičević is with the Department of Energy Technology, Aalborg University, 9220 Aalborg East, Denmark (e-mail: tdr@ et.aau.dk).

Color versions of one or more of the figures in this article are available online at http://ieeexplore.ieee.org.

Digital Object Identifier 10.1109/TPEL.2019.2962838

I. INTRODUCTION

DC MICROGRID has its applications in vehicles [1], vessels [2], and aircrafts [3] under the initiative of the transportation electrification. Energy storage systems (ESS) are often demanded in those system to provide intermittent power through the interface of isolated dc–dc converters. Dual-active bridge (DAB) and its derived topologies [4]–[6] have drawn considerable attention in these applications [7], [8]. They provide salient merits in high-frequency galvanic isolation, high-voltage step up/down ability and high-power conversion efficiency.

SPS is the most widely used modulation in the DAB due to its simplicity [9]–[12]. When the voltage gain deviates from unity, the SPS-modulated DAB can have high circulating current and lose zero voltage switching ON, which will decrease the efficiency significantly [13]. Various hardware and control methods have been proposed to solve these problems, among them, adjusting duty cycles of H-bridges are the most effective approach [13]. Based on the number of the phase-shift ratios, these methods can be classified as extended phase shift (EPS) [14], dual-phase shift (DPS) [15], and triple-phase shift (TPS)

[16]. Compared with EPS or DPS, the TPS utilizes all the three phase-shift ratios and can maximize the efficiency.

In the existing literature, the control of DAB is mainly focused on the DAB modulated using the SPS (SPS-DAB) [17]–[21]. The control of TPS-DAB is barely addressed in the existing literatures due to its complexity. Since there are many different operating modes and three phase-shift ratios, the variant small-signal model of the TPS-DAB requires the PI controllers to be designed and tuned at each equilibrium points. Otherwise the performance will be deteriorated. The parameter design becomes complex when the converter has a wide operating voltage range. Huang *et al.* [22] employed two slow PI controllers for the inner phase shifts to avoid oscillation and instability during transitions when using TPS. However, this significantly reduced the bandwidth of control. Wu *et al.* [23] addressed the stability issue with TPS using Lyapunov function. Each operating stage was treated separately which was inept at design guidance for the control parameters.

Predictive control is often considered in power electronics converters for several advantages it can provide, such as fast dynamics, easy inclusion of constraints, and simple digital implementation. In particular, finite-control set model-predictive control (FCS-MPC) has been investigated in ac power conversion [24]–[26]. In contrast, the application of predictive control in dc/dc converters has not been so intensively explored; FCS-MPC methods proposed for use in the boost converter with receding horizon by Karamanakos *et al*. [17] and Wang *et al*. [18] demonstrated fast dynamics. However, these approaches resulted in variable switching frequency and demanded heavy computation. Oettmeier *et al*. [19] proposed a continuous control set model-predictive control (CCS-MPC) also for boost converters which effectively avoided voltage transition overshoot. Notwithstanding, abovementioned approaches are not applicable in TPS-DAB.

In this article, the control variable in TPS-DAB is discretized into finite elements to fit in the concept of the well-known FCS-MPC. The proposed moving discretized control set model-predictive control (MDCS-MPC) has the merits listed as follows.

1) Circuit parameters, terminal voltages, and operating modes of TPS-DAB are embedded in the prediction model. Therefore, control parameters designed for MDCS-MPC can provide good performance throughout the power and terminal voltage range.
2) The proposed approach enables flexible multiobjective optimization. With the proposed method, similar dc microgrid stabilization control typically seen with FCS-MPC can also be applied to TPS-DAB [27].
3) Compared to previous applications of FSC-MPC in dc–dc converters [17], [18], MDCS-MPC utilizes only two prediction horizons and a small number of calculating points in each switching period. Therefore, the computational burden is relatively low.

This article is organized as follows. In Section II, the concept of TPS modulation is presented. The small-signal modeling and the conventional PI control for TPS-DAB have been introduced. In Section III, the MDCS-MPC is proposed. The ideal discretised model is derived. Operating principle is intuitively introduced. The cost function and the adaptive step concept have also been set forth. Multiobjective control based on the proposed control concept is illustrated. In the next section, the causes of the steady-state error for the proposed MDCS-MPC have been analyzed in development of a compensation method. In Section V, experimental results are conducted on a 20 kHz, 1 kW DAB converter, validating theoretical claims. Finally, Section VI concludes this article.

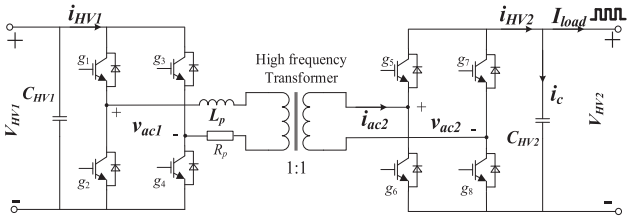

Fig. 1. Diagram of the DAB converter under investigation.

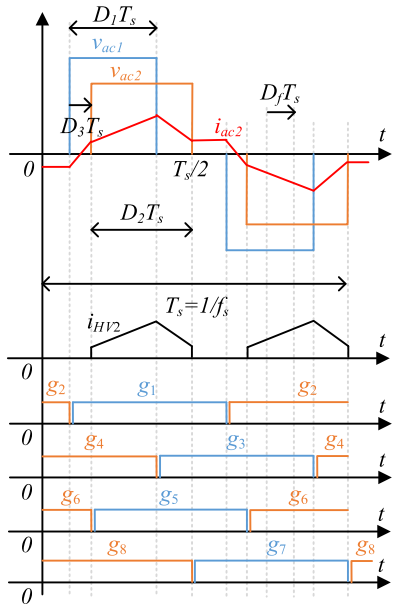

Fig. 2. Generic waveforms of the DAB modulated with TPS.

II. Analysis on TPS-DAB

The diagram of the DAB converter is shown in Fig. 1. H-bridges on each side of the high-frequency transformer generate square voltages v_{ac1} and v_{ac2} with a fundamental frequency of f_s. They are exerted on the power transferring inductor L_p, producing transformer current i_{ac2}. T_s denotes one switching period.

As depicted in Fig. 2, D_1T_s, D_2T_s are the active state time periods of v_{ac1} and v_{ac2}. When the SPS is applied [10], active states duties D_1 and D_2 are fixed at 0.5, whereas the phase shift D_fT_s between v_{ac1} and v_{ac2} is controlled to transfer the power between primary and secondary sides.

A. Offline Optimization on TPS-DAB

The DAB converter has four control variables. They are D_1, D_2, D_f, and f_s. In TPS, the phase-shift ratios D_1, D_2, and D_f are regarded as three independent control variables while f_s is

TABLE I
MINIMIZATION ON REACTIVE POWER [16], $r_V = V_{HV2}/V_{HV1}$

Gain	D_f range	Relationships	Mode
$r_V<1$	$[0, \frac{1-r_V}{4}]$	$D_1 = \frac{2r_V}{1-r_V}D_f,\ D_2 = \frac{2}{1-r_V}D_f,\ D_3 = 0$	I
	$(\frac{1-r_V}{4}, \frac{1}{4}]$	$D_1 = \frac{2r_V-1}{2r_V} + \frac{1-r_V}{r_V}D_f,\ D_2 = 0.5,\ D_3 = \frac{r_V+4D_f-1}{4r_V}$	II
$r_V>1$	$[0, \frac{r_V-1}{4r_V}]$	$D_1 = \frac{2r_V}{r_V-1}D_f,\ D_2 = \frac{2}{r_V-1}D_f,\ D_3 = 2D_f$	III
	$(\frac{r_V-1}{4r_V}, \frac{1}{4}]$	$D_1 = 0.5,\ D_2 = 1-0.5r_V+2(r_V-1)D_f,$ $D_3 = (2-r_V)D_f + 0.25(r_V-1)$	IV

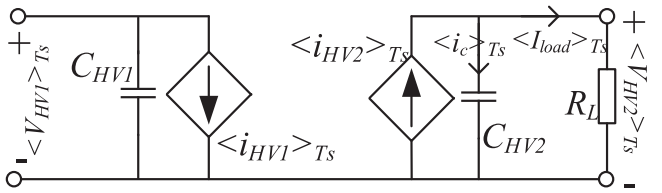

Fig. 3. Averaged model of the DAB.

fixed. To minimize the circulating current, authors in [16], [28], and [29] have derived the optimal phase-shift ratios, as shown in Table I.

D_f is the only independent control variable, whereas D_1 and D_2 can be calculated using D_f. The gate signals g_1–g_8 can be then generated according to Fig. 2. Although the TPS modulation has its advantages, the complexity in control design hinders its application in practice. As shown in Table I, there are four operating modes, the small-signal model of TPS-DAB varies with operating modes, terminal voltages, and power.

B. Modeling of the TPS-DAB

The accurate switching averaged models of the DAB have been intensively investigated by researchers [29], [30]. However, those models of DAB draw on the most straightforward SPS modulation. When it comes to the TPS, the utilization of inner phase shifts and the coexistence of different operation modes make the accurate switching average model complicated. In this article, a simplified averaged model of the DAB is used, as shown in Fig. 3.

The controlled current $< i_{HV2} >_{Ts}$ is calculated from (1). Substituting Table I into (1), the expressions for each operating mode are derived, as in Table II

$$< i_{HV2} >_{Ts} = \frac{1}{T_s}\int_0^{T_s} i_{HV2}dt. \tag{1}$$

The differential equation of the output voltage is developed from Fig. 3 as follows:

$$\frac{d < V_{HV2} >_{Ts}}{dt} = \frac{< i_{HV2} >_{Ts}}{C_{HV2}} - \frac{< V_{HV2} >_{Ts}}{R_L C_{HV2}}. \tag{2}$$

TABLE II
SWITCHING AVERAGED MODEL UNIFIED AT $V_{HV1}/(8f_sL_p)$

Mode	$<i_{HV2}>_{Ts}$
I	$\frac{32r_V D_f^{\,2}}{1-r_V}$
II	$\frac{-8(r_V^{\,2}+1)D_f^{\,2} + 4(2r_V^{\,2} - r_V + 1)D_f - (r_V-1)^2}{r_V^{\,2}}$
III	$\frac{32D_f^{\,2}}{r_V - 1}$
IV	$-16(r_V^{\,2} - 2r_V + 2)D_f^{\,2} + 8(r_V^{\,2} - 2r_V + 2)D_f - (r_V-1)^2$

TABLE III
OPEN-LOOP CONTROL TO OUTPUT TRANSFER FUNCTION

Mode	$G_{TPS}(s) = V_{HV2}(s)/D_f(s)$
I	$G_{TPS\_I}(s) = \frac{8\overline{D_f}\overline{V_{HV1}}\overline{r_V}R_L(1-\overline{r_V})}{C_{HV2}f_sL_pR_L(1-\overline{r_V})^2 s - 4R_L\overline{D_f}^{\,2} + f_sL_p(\overline{r_V}^{\,2} - \overline{r_V} + 1)}$
II	$G_{TPS\_II}(s) = -\frac{2R_L\overline{V_{HV1}}\overline{r_V}(4\overline{D_f} + \overline{r_V} + 4\overline{D_f}\overline{r_V}^{\,2} - 2\overline{r_V}^{\,2} - 1)}{4C_{HV2}f_sL_pR_L\overline{r_V}^{\,3}s - 8R_L\overline{D_f}^{\,2} - 2R_L\overline{D_f}\overline{r_V} + 4R_L\overline{D_f} + 4f_sL_p\overline{r_V}^{\,3} + R_L\overline{r_V} - R_L}$
III	$G_{TPS\_III}(s) = \frac{8\overline{D_f}\overline{V_{HV1}}R_L(\overline{r_V}-1)}{sC_{HV2}f_sL_pR_L(1-\overline{r_V})^2 + 4R_L\overline{D_f}^{\,2} + f_sL_p(1-\overline{r_V})^2}$
IV	$G_{TPS\_IV}(s) = \frac{-4R_L\overline{V_{HV1}}(4\overline{D_f} - 1)(\overline{r_V}^{\,2} - 2\overline{r_V} + 2)}{4C_{HV2}f_sL_pR_Ls + 4f_sL_p - R_L + R_L\overline{r_V} - 16\overline{D_f}^{\,2}R_L + 8\overline{D_f}R_L - 8\overline{D_f}\overline{r_V}R_L + 16\overline{D_f}^{\,2}\overline{r_V}R_L}$

Note: The notation with a bar $\bar{X}$ denotes the equilibrium points.

TABLE IV
CIRCUIT AND CONTROL PARAMETERS

Description	Value	Units
Switching frequency f_s	20	kHz
Dead time t_d	1.6	μS
Transformer turn ratio	20:20	/
Primary power inductor L_p	300	μH
Parasitic resistance R_p	50	mΩ
Primary DC capacitor C_{HV1}	380	μF
Secondary DC capacitor C_{HV2}	380	μF
Rated power	1	kW
Adaptive step saturate V_m	10	V
Adaptive step factor λ	1	/
Searching points μ	11	/
Weighting factor α_1	1	/
Weighting factor α_2	4	/
Proportional coefficient K_p	0.05	/
Integral coefficient K_i	3.57	/
Feedforward coefficient K_f	0.01	/

The small-signal models are derived by superimposing small perturbations on the equilibrium points. The control to output transfer functions for TPS-DAB are provided in Table III.

In order to verify the correctness of the control to output transfer functions $G_{\mathrm{TPS}}(\mathrm{s})$ listed in Table III, simulations have been conducted using the software PLECS block set 3.6.1 built in with MATLAB SIMULINK 2017a. The converter parameters are provided as in Table IV, otherwise specified.

Comparisons between the math models in Table III and the ac swept transfer functions $G_{\mathrm{TPS}}(s)$ based on the ideal averaged model in Fig. 3 are carried out. The ac sweeping diagram with the ideal model is depicted in Fig. 4. Sinusoidal small perturbations are injected and superimposed on the equilibrium value of $\overline{D_f}$.

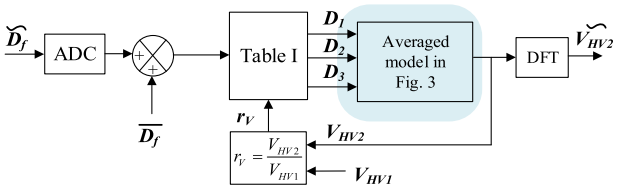

Fig. 4. Transfer function ac sweeping diagram with the averaged model.

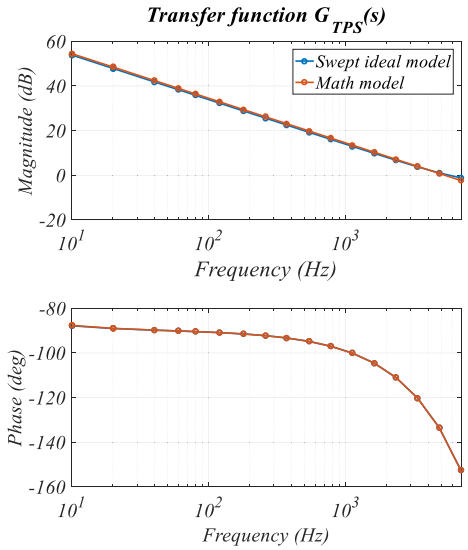

Fig. 5. Comparison between the ac swept ideal model and the math model in Table III under 260 V/300 V 10 W Mode III.

Correspondent frequency components of the output voltage are measured. The open-loop control to output transfer function can then be calculated as

$$G_{\mathrm{TPS}}(f) = \frac{V_{HV2}(f)}{D_f(f)}. \tag{3}$$

The results are illustrated in Fig. 5. The math model agrees well with the swept ideal model. This confirms the correctness of the math model in Table III. It is worth mentioning that the ideal model is a first-order system. Ideally, the phase should be always $-90°$. However, as shown in Fig. 5, the phase is larger than $-90°$ in low frequency due to the impact from R_L. The phase is smaller than $-90°$ in high frequency due to the digital sampling delay reflected as $e^{-s/2fs}$ in multiplication to transfer functions from Table III.

C. PI Control for TPS-DAB

With the abovementioned developed transfer function in Table III, a PI voltage control with load current feedforward structure is utilized as a comparison benchmark. Sampling of the output voltage V_{HV2} and load current I_{load} are required. The PI voltage controller is defined as

$$Gv(s) = K_p + \frac{K_i}{s}. \tag{4}$$

The simplified control block diagram is depicted in Fig. 6. The transfer function G_{TPS}(s) is variant with the operating terminal

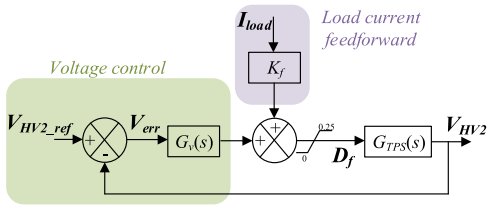

Fig. 6. PI control block diagram.

voltages and power. Moreover, due to the coexistence of four operating modes, the PI controller parameter design becomes overwhelming. In the following sections, PI parameters K_p and K_i, defined in (4), are only designed and tuned at the points of interest for comparison purpose.

D. Remarks on the Design Issues With PI

When the TPS modulation is applied to DAB converters. The small-signal model of the TPS-DAB is variant. It depends on the operating modes, terminal voltages, and load power. In a single point of operation, the PI controller can be easily designed and tuned. However, when the converter operating condition is changed, the performance will be deteriorated. This phenomenon will be addressed in Section III-B. Considering there are many operating modes in TPS-DAB, it is complex to optimally design the control parameters for TPS-DAB working in a wide terminal voltages and power range.

To address the abovementioned issue, this article develops a controller for the TPS-DAB with the information of terminal voltages and circuit parameters embedded in the algorithm. The proposed controller presents better global dynamic performance with easier parameter tuning compared with the conventionally PI controller for TPS-DAB.

III. Proposed MDCS-MPC

The main objective of the control in the case of study is to regulate the bus voltage V_{HV2} supplying power to resistive loads. Based on the averaged model described in Fig. 3, the discretized difference equation of the output voltage is developed as follows:

$$V_{HV2}[k+1] = \frac{i_{HV2}[k+1] - I_{\mathrm{load}}[k+1]}{C_{HV2} f_s} + V_{HV2}[k]. \tag{5}$$

When the converter is loaded with the passive loads, the future load current is unknown. However, for a two-step prediction, the future load current is essential to predict voltage values of V_{HV2} at time instance $k+2$. Therefore, an assumption has been made that load current does not vary drastically in two sampling periods. This assumption has also been commonly used in MPC controlled inverters [27], [31]

$$I_{\mathrm{load}}[k] = I_{\mathrm{load}}[k+1] = I_{\mathrm{load}}[k+2]. \tag{6}$$

The prediction for output voltage at time instance $k+2$ is

$$V_{HV2}[k+2] = \frac{i_{HV2}[k+2] - I_{\mathrm{load}}[k]}{C_{HV2} f_s} + V_{HV2}[k+1]. \tag{7}$$

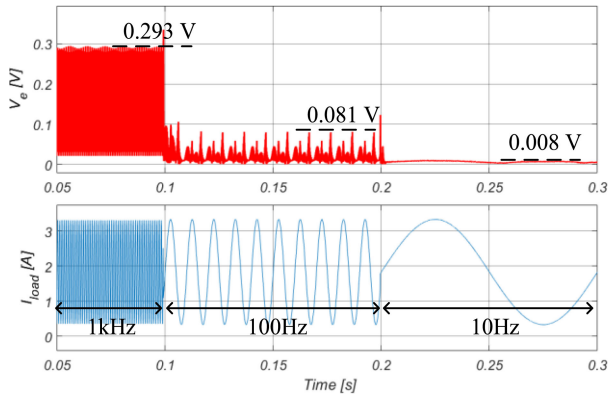

Fig. 7. Voltage prediction error evaluation.

Substituting (5) into (7) yields

$$V_{HV2}[k+2] = \frac{i_{HV2}[k+2] + i_{HV2}[k+1] - 2I_{\text{load}}[k]}{C_{HV2} f_s} + V_{HV2}[k] \tag{8}$$

where $i_{HV2}[k+1]$ and $i_{HV2}[k]$ can be easily derived from Table II.

In order to evaluate how realistic the assumption made in (6) is, and how accurate the prediction in (8) is, the prediction error has been defined in the following equation as a metric

$$V_e = |V_{HV2}[k+2] - V_{HV2\_s}[k+2]| \tag{9}$$

where $V_{HV2\_s}[k+2]$ is the sampled load voltage at time instance $k+2$. A sinusoidal controlled current source is connected to the output terminal with a fixed amplitude but varying frequency. In (6), the load current is assumed to be constant within two sampling periods. Therefore, when the load current changes slowly, this assumption is more likely to hold true. The results shown in Fig. 7 have verified this statement. When the load current has a frequency of 1 kHz, the maximum prediction error is 0.293 V. With the decreasing of the frequency down to 10 Hz, the maximum prediction error is reduced to 0.008 V. The error in the prediction will not necessarily cause problems. Since 1 kHz is already above the bandwidth, 0.293 V error is only 0.09% of rated voltage. Therefore, the assumption (6) has been deemed reasonable in our case of study.

A. Operating Principle

The proposed MDCS-MPC controls the converter output voltage V_{HV2} based on the discretized average model of the DAB in Fig. 3. Taking into account the computational delay, MDCS-MPC has a prediction step of two sampling periods. A preliminary cost function is proposed, as in (10), with the only purpose of regulating voltage V_{HV2} to reference V_{HV2_ref}. It is worth mentioning that (10) is not the finalized cost function, but a simple one meant to help illustrate the operating principle of the proposed MDCS-MPC

$$ct = (V_{HV2\_\text{ref}} - V_{HV2}[k+2])^2. \tag{10}$$

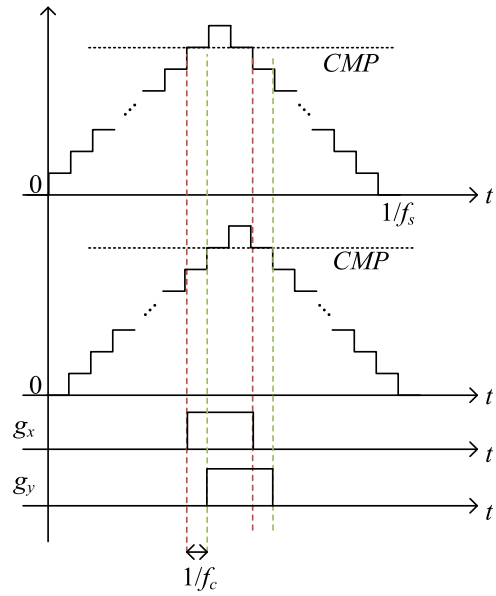

Fig. 8. Demonstration of the finest phase-shift value in PWM modules.

It should be noted that according to Tables I and II, there is only one control variable D_f rather than three. The variable D_f is continuous in nature. However, in digital control, D_f needs to be discretized. The discretization precision is subjected to the control platform applied. Δ_f is defined in (11) as the finest phase-shift value that can be achieved in a digital control platform, as shown in Fig. 8

$$\Delta_f = \frac{f_s}{f_c} \tag{11}$$

where f_c is the peripheral clock frequency of the digital control platform. For unidirectional power flow, DAB works predominately in the range

$$D_f \in [0, 0.25]. \tag{12}$$

Equation (12) is further discretized into $\mu_m (= 0.25/\Delta_f + 1)$ elements, as described in the following array:

$$D_f \in \{0, \Delta_f, 2\Delta_f, \ldots, 0.25\}. \tag{13}$$

In order to implement a control algorithm that is feasible on standard commercial microcontrollers, the proposed MDCS-MPC evaluates a reduced number of values in each sampling period. In one sampling period, μ ($\mu \leq \mu_m$) number of points are assessed. They are centered at the previous working point.

An intuitive illustration of the proposed MDCS-MPC is depicted in Fig. 9. In the control interval k to $k+1$, $\mu = 3$ points are evaluated centred at the previous working point $D_f[k] = a$. When $D_f[k+1]$ equals $a - \Delta_f$, a, and $a + \Delta_f$, the output voltage V_{HV2} is predicted as $V^{(1)}_{HV2}[k+2]$, $V^{(2)}_{HV2}[k+2]$, and $V^{(3)}_{HV2}[k+2]$, respectively. The superscript represents the index of an element in the moving discretized control set.

The moving discretized control set during the period k to $k+1$ is $\{a - \Delta_f, a, a + \Delta_f\}$. According to the illustration in Fig. 9, when $D_f[k+1] = a + \Delta_f$, the predicted output voltage

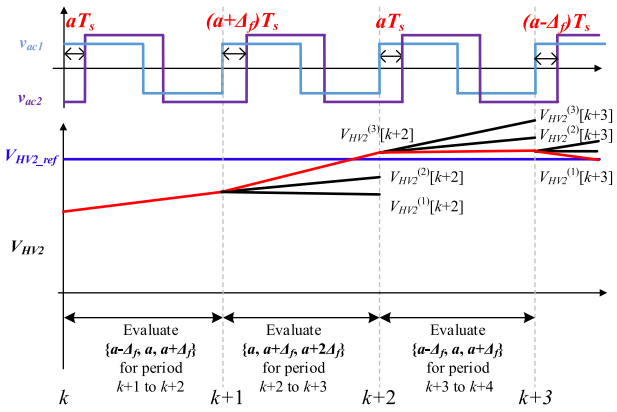

Fig. 9. Operating principle of the proposed MDCS-MPC for DAB. μ is set to be 3 for illustration.

$V_{HV2}^{(3)}[k+2]$ is the closest to V_{HV2_ref}. This results in the smallest cost function defined in (10). Therefore, the value $a+\Delta_f$ is applied at time instance $k+1$ to D_f. In the next control interval, the same process is repeated. However, the moving discretized control set has changed. It has become $\{a,\ a+\Delta_f,\ a+2\Delta_f\}$. The control set is moving with the working point within the domain of (13). In this control interval, $D_f[k+3]=a$ results in the smallest cost function. Therefore, this value is applied at the time instance $k+2$. This process goes on.

Larger value of μ can increase the transition dynamics, but it aggravates the computational burden to the real-time digital controller. Therefore, an adaptive step for D_f is adopted instead of the finest search step Δ_f. Define the adaptive step Δ_{adp}, as (15) and (16). The adaptive step Δ_{adp} changes with the deviation of the output voltage to the reference. When V_{HV2} is far from the reference, Δ_{adp} grows large. In contrast, when V_{HV2} equals to the reference, Δ_{adp} becomes $\Delta_{f.}$. Such that the control accuracy remains

$$V_\Delta=\begin{cases}|V_{HV2\_\mathrm{ref}}-V_{HV2}[k]|\,, & |V_{HV2\_\mathrm{ref}}-V_{HV2}[k]|<V_m\\ V_m, & |V_{HV2\_\mathrm{ref}}-V_{HV2}[k]|>V_m\end{cases} \tag{14}$$

$$\Delta_{\mathrm{adp}}=\Delta_f(1+\lambda V_\Delta^2) \tag{15}$$

where V_m is the saturated voltage, λ is a coefficient determined according to the requirement of transition performance, λ and V_m are set as 1 and 10 V, respectively, in the following simulation and experiment validations.

B. Proposed Cost Function

In order to help the system to converge, a second term G_2 is proposed in the cost function as follows:

$$ct=\alpha_1 G_1+\alpha_2 G_2 \tag{16}$$

where

$$\begin{cases}G_1=(V_{HV2\_\mathrm{ref}}-V_{HV2}[k+2])^2\\ G_2=(V_{HV2}[k+2]-V_{HV2}[k])^2.\end{cases} \tag{17}$$

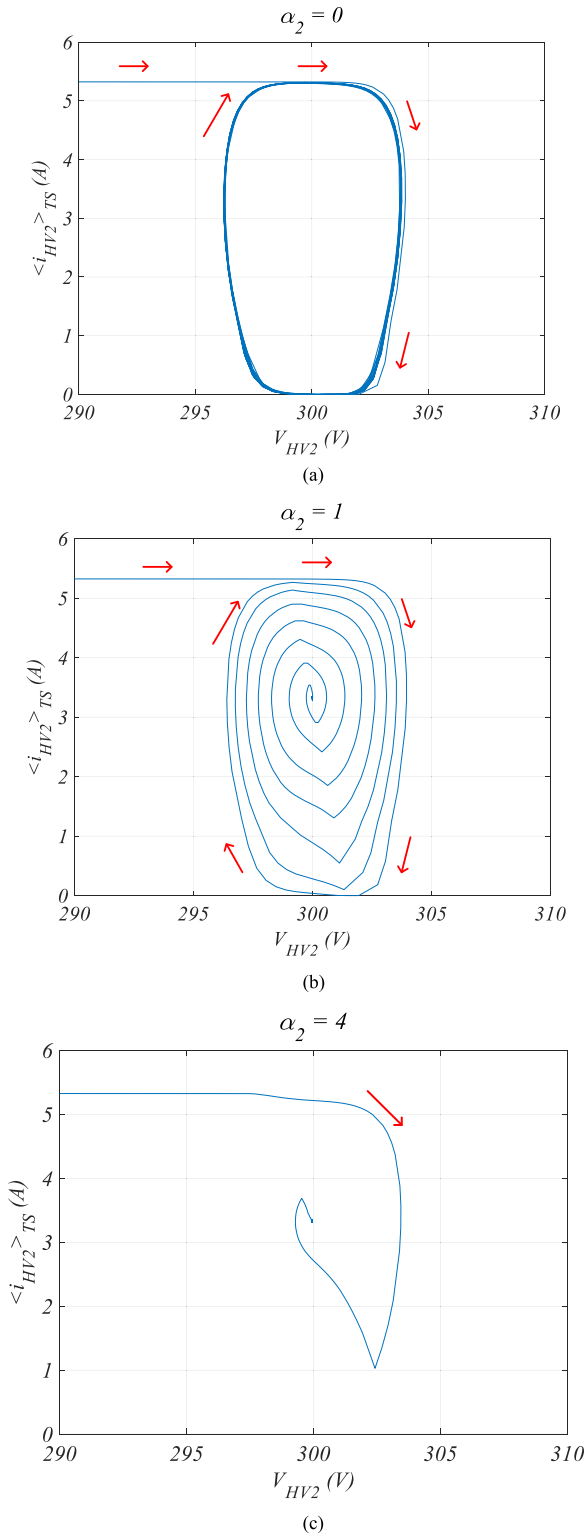

Fig. 10. Phase portrait with different α_2.

The first term G_1 is responsible for regulation of the output voltage V_{HV2} to reference value V_{HV2_ref}, whereas the second term G_2 takes charge of the system convergence. Fig. 10 shows how the weighting factor α_2 affects the convergence of bridge current $<i_{HV2}>_{Ts}$ and load voltage V_{HV2}. The value of α_2 has a positive effect on the system convergence. When α_2 is zero,

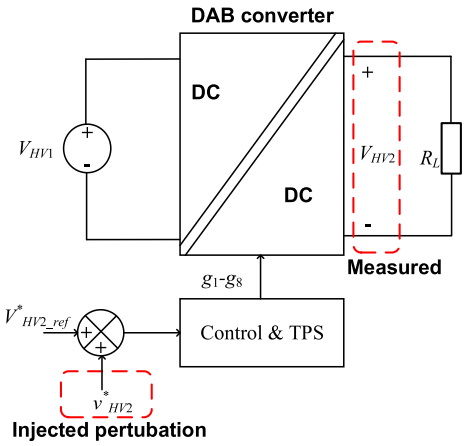

Fig. 11. Frequency-response sweeping circuit.

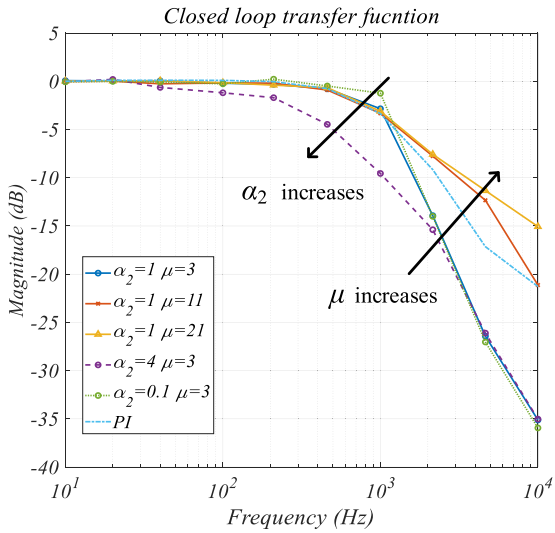

Fig. 12. Sweeping results for $G_{R2O}(f)$ in (18) under equilibrium point 260 V/300 V 1 kW.

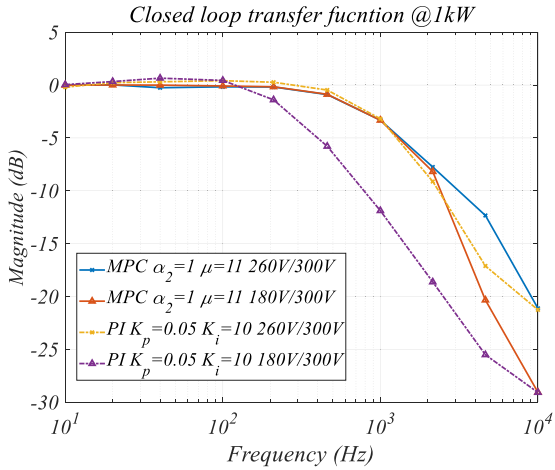

Fig. 13. Frequency response with different input voltage.

the system does not converge. However, α_2 cannot be set too large because it has negative impact on the control bandwidth. This will be addressed later in this section.

In order to provide a quantitative assessment on the performance of MDCS-MPC using the cost function in (16), the frequency response is utilized. The small-signal models of DAB converters are often carried out to analytically derive its frequency response. However, this is infeasible to describe the DAB converters with nonlinear controllers. Another approach is utilized here. If a certain small sinusoidal perturbation signal that is applied to a nonlinear element always excites a sinusoid at the same frequency in the output, then such an element can be represented by its linear "equivalent" frequency response, which is commonly called a describing function (see [32, ch. 5]). As a result, standard frequency domain techniques can be used to assess the characteristics of the converter that comprises nonlinear elements [27]. The same as the analytical method (small-signal modeling), the describing function method also needs to have its assessments carried out based on a given equilibrium point. Small-signal perturbations have been injected to the converter and responses have been measured with the correspondent frequency. This numerical method applies to both linear and nonlinear controls.

The ac sweepings are carried out in the switching model under the equilibrium point 260 V/300 V 1 kW. Perturbations from 10 Hz to 10 kHz with amplitude of 0.01 V are superimposed on the output voltage equilibrium value $V_{HV2\_\mathrm{ref}} = 300$ V, as shown in Fig. 11. The closed-loop transfer function is defined as

$$G_{R2O}(f) = \frac{V_{HV2}(f)}{v^*_{HV2}(f)}. \tag{18}$$

The results are presented in Fig. 12. In the figure, the closed-loop transfer functions in the frequency domain with different values of α_2 and μ are shown. In observation of the solid lines ($\alpha_2 = 1$), μ increases the amplitude of $G_{R2O}(f)$ in the high-frequency range. When comparing lines with round markers ($\mu = 3$), it can be concluded that α_2 has a negative impact to the amplitude of $G_{R2O}(f)$ in the low- to medium-frequency range. Parameters α_2 and μ have clear implications on $G_{R2O}(f)$. The PI parameters are designed based on the ideal/math model under the equilibrium point 260 V/300 V 1 kW. The control parameters are designed as $K_p = 0.05$ and $K_i = 10$. The gain and phase margins are 15.4 dB and 72 deg, respectively. The crossover frequency is 570 Hz. As shown in the figure, the frequency response line of PI sits between the blue and red lines of MDCS-MPC. If tuned with $\alpha_2 = 1$ and a μ between 3 and 11, the MDCS-MPC can present very similar frequency response as the designed PI.

In order to guarantee the performance, the control parameters of the PI controller have to be designed based on a single equilibrium point. When the operating point varies, $G_{R2O}(f)$ will change as well. For example, as shown in Fig. 13, with the PI controller, when the input voltage V_{HV1} reduces from 260 V (yellow line) to 180 V (purple line), the amplitude of $G_{R2O}(f)$ varies significantly. In comparison, when MDCS-MPC is used, $G_{R2O}(f)$ can largely maintain.

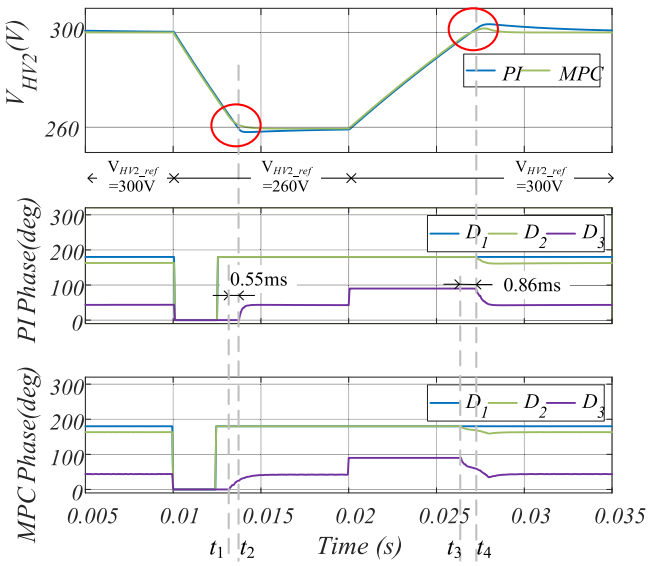

Fig. 14. Load-voltage reference tracking.

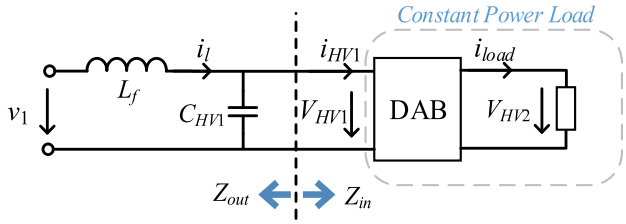

Fig. 15. DAB with an input *LC* filter.

The abovementioned phenomenon about PI controller and MDCS-MPC can also be confirmed in experiments Figs. 21 and 22.

The reference tracking performance of the PI and the proposed method in the time domain has also been compared. As shown in Fig. 14, the load-voltage reference changes between 300 and 260 V. At time instance t_1, when the proposed control is used, D_3 starts to increase 0.55 ms before V_{HV2} reaches the reference 260 V. In contrast, when PI is used, D_3 can only start to increase once V_{HV2} reaches 260 V. The similar phenomenon can also be observed at time instances t_3 and t_4. The feature ensures MDCS-MPC to provide better voltage tracking performance. This phenomenon is also confirmed in experiment Figs. 25 and 26.

C. Flexible Multiobjective Control

The proposed MDCS-MPC can be extended to applications where multiobjective control is required. Control objectives can be coordinately achieved by adding terms in the cost function as with FCS-MPC [27].

In order to demonstrate this benefit, apart from the regulation of the output voltage V_{HV2}, the DAB is assigned also another task to stabilize the input voltage V_{HV1} in presence of oscillation due to the well-known constant power load stability issue [33]. A DAB converter with an input *LC* filter is illustrated in Fig. 15 to showcase the scenario.

Instability could happen when $Z_{\text{out}}/Z_{\text{in}}$ does not satisfy the impedance-based Nyquist stability criterion [34]. Therefore, stabilization control is required. The cost function is then proposed as

$$ct = \alpha_1 G_1 + \alpha_2 G_2 + \alpha_3 G_3 \tag{19}$$

where

$$G_3 = (V_{HV1}[k+2] - v_1[k])^2 \tag{20}$$

$$V_{HV1}[k+2] = \frac{2I_{\text{load}}[k] - (i_{HV1}[k+2] + i_{HV1}[k+1])}{C_{HV2} f_s} + V_{HV1}[k]. \tag{21}$$

The only difference between the calculation of the current i_{HV1} and i_{HV2} is that i_{HV1} is unified at $V_{HV2}/(8f_sL_p)$, whereas i_{HV2} is unified at $V_{HV1}/(8f_sL_p)$ in Table II.

The effectiveness of the stabilization term G_3 has been verified in the experiment Section V-C. Since this article focuses only on the proposal of the MDCS-MPC idea in TPS-DAB, and scenario in Fig. 15 is only used to showcase the capability of MDCS-MPC. Further detailed analysis on system stabilization is not discussed.

IV. Steady-State Error Analysis

Two causes for the steady-state error specifically in the proposed MDCS-MPC are addressed in this section. Relevant error compensation approaches are elaborated.

The first cause is the prediction error from the ideal model. As stated earlier in Section II, the accurate modeling of the DAB modulated with TPS is rather complicated. The simplified reduced order model in Fig. 3 enables relatively easier implementation; however, it also brings perdition error in $< i_{HV2} >_{Ts}$.

The second cause is the contradiction between G_1 and G_2. When V_{HV2} reaches close to V_{HV2_ref}, G_1 becomes very small. The predicted step change $(V_{HV2}[k+2] - V_{HV2}[\text{k}])$ is higher than the steady-state error $(V_{HV2\_\text{ref}} - V_{HV2}[k+2])$. In this case, the decreasing of $\alpha_1 G_1$ does not compensate for the increasing of $\alpha_2 G_2$. $(V_{HV2\_\text{ref}} - V_{HV2}[k+2])$ cannot be zero, therefore causing the steady-state error.

A. Error Caused by the Prediction Model

The error of the ideal prediction model in Table II can be corrected by a compensation term defined as I_{comp} in (22). I_{comp} is calculated as the difference between the observed output current value i_{HV2_r} and the predicted value i_{HV2}

$$I_{\text{comp}}[k] = i_{HV2\_r}[k-1] - i_{HV2}[k-1] \tag{22}$$

where

$$i_{HV2\_r}[k-1] = \frac{C_{HV2}}{T_s}(V_{HV2}[k] - V_{HV2}[k-1]) + I_{\text{load}}[k-1]. \tag{23}$$

The correction of the prediction model can eliminate the steady-state error for the output voltage. However, due to the calculation of i_{HV2_r} in (23) involves derivative of V_{HV2}. In presence of sampling noise, the compensation term I_{comp} could

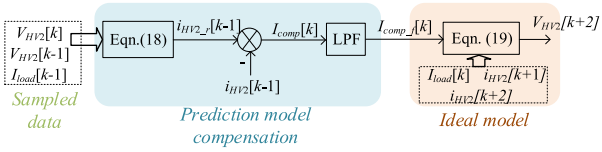

Fig. 16. Compensation diagram for the prediction error.

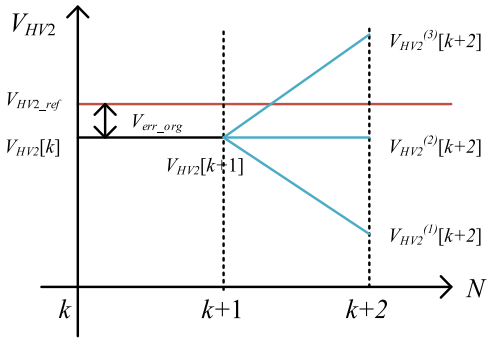

Fig. 17. Illustration of the steady state error.

deteriorate the dynamic performance of MDCS-MPC. I_{comp} is designed solely for the purpose of steady-state error correction. A low-pass filter (LPF) can be applied for I_{comp}. Therefore, the predicted output voltage is modified as in (24). A diagram of the compensation for the prediction error is shown in Fig. 16. A moving average filter is used as the LPF. The effectiveness of the prediction error compensation is verified by both simulations and experiments in Sections V and VI

$$V_{HV2}[k+2] = \frac{i_{HV2}[k+2] + i_{HV2}[k+1] + 2I_{\text{comp\_}f}[k] - 2I_{\text{load}}[k]}{C_{HV2}f_s} + V_{HV2}[k]. \tag{24}$$

B. Error Caused by the Weighting Factor α_2

In this section, the steady-state error caused by the weighting factor α_2 is analyzed. To start with, consider the initial cost function in (10) without G_2 and assume that the converter has already been in the steady state

$$V_{HV2}[k] = V_{HV2}[k+1] \tag{25}$$

$$I_{\text{load}}[k] = i_{HV2}[k] = i_{HV2}[k+1] \tag{26}$$

where the steady-state error $V_{\text{err\_org}}$ is defined as

$$V_{\text{err\_org}} = V_{HV2\_\text{ref}} - V_{HV2}[k]. \tag{27}$$

Substitute the conditions (26) and (27) into the prediction model (8). The prediction value for the output voltage $V_{HV2}^{(3)}[k+1]$ in Fig. 17 is

$$V_{HV2}[k+2] = \frac{i_{HV2}[k+2] - i_{HV2}[k+1]}{C_{HV2}f_s} + V_{HV2\_\text{ref}} - V_{\text{err\_org}}. \tag{28}$$

Equation (28) can be further modified as

$$V_{HV2}[k+2] = \frac{\Delta_{\text{adp}}}{C_{HV2}f_s}\frac{di_{HV2}}{dD_f}|_{Df=\overline{Df}} + V_{HV2\_\text{ref}} - V_{\text{err\_org}}. \tag{29}$$

The cost functions with voltage predictions $V_{HV2}^{(2)}[k+2]$ and $V_{HV2}^{(3)}[k+2]$ are

$$ct^{(2)} = V_{\text{err\_org}}^2 \tag{30}$$

$$ct^{(3)} = \left(\frac{\Delta_{\text{adp}}}{C_{HV2}f_s}\frac{di_{HV2}}{dD_f}|_{Df=\overline{Df}} - V_{\text{err\_org}}\right)^2. \tag{31}$$

Due to the steady-state assumption, (32) has to hold true

$$ct^{(2)} < ct^{(3)}. \tag{32}$$

Therefore, the maximum prediction error $V_{\text{err\_org\_max}}$ can be obtained as

$$V_{\text{err\_org}} < \frac{\Delta_{\text{adp}}}{C_{HV2}f_s}\frac{di_{HV2}}{dD_f}|_{Df=\overline{Df}} = V_{\text{err\_org\_max}}. \tag{33}$$

Now, consider the cost function defined in (16) with the second term G_2 enabled. Set $\alpha_1 = 1$. The cost functions with the voltage prediction $V_{HV2}^{(2)}[k+2]$ and $V_{HV2}^{(3)}[k+2]$ become

$$ct^{(2)} = V_{\text{err\_ mod}}^2 \tag{34}$$

$$ct^{(3)} = \left(\frac{\Delta_{\text{adp}}}{C_{HV2}f_s}\frac{di_{HV2}}{dD_f}|_{Df=\overline{Df}} - V_{\text{err\_ mod}}\right)^2 + \alpha_2\left(\frac{\Delta_{\text{adp}}}{C_{HV2}f_s}\frac{di_{HV2}}{dD_f}|_{Df=\overline{Df}}\right)^2 \tag{35}$$

where $V_{\text{err\_mod}}$ is the steady-state error with the term G_2 enabled.

Due to the steady-state assumption, substitute (33)–(35) in (32), the maximum prediction error $V_{\text{err\_mod\_max}}$ becomes

$$V_{\text{err\_ mod}} < V_{\text{err\_org\_max}}(1+\alpha_2) = V_{\text{err\_mod\_max}}. \tag{36}$$

The steady-state error is dependent on the working points of the converter such as power and the terminal voltage ratio. The conclusion can be drawn from (33) that smaller the step Δ_{adp}, bigger the output capacitor C_{HV2}, and higher the switching frequency f_s are conducive for the reduction on the voltage steady-state error. It also can be concluded from (36) that the existence of α_2 increases the original steady-state error $V_{\text{err\_org\_max}}$ with only G_1 in the cost function by a multiplier of $(1+\alpha_2)$. Higher values of α_2 introduces higher attenuation to sampling noise and damping effect; however, it may slow down the dynamic and cause larger steady-state output voltage error.

In applications typically with large output capacitor and high switching frequency, the error is small enough to be neglected. However, in some cases where high voltage precision is required, the adaptive weighting factor design proposed by Dragicevic [35] can be adopted to address the issue.

V. Experimental Results

The proposed methodology has been validated on a 1-kW 20-kHz laboratory prototype. The load R_L is switched ON and

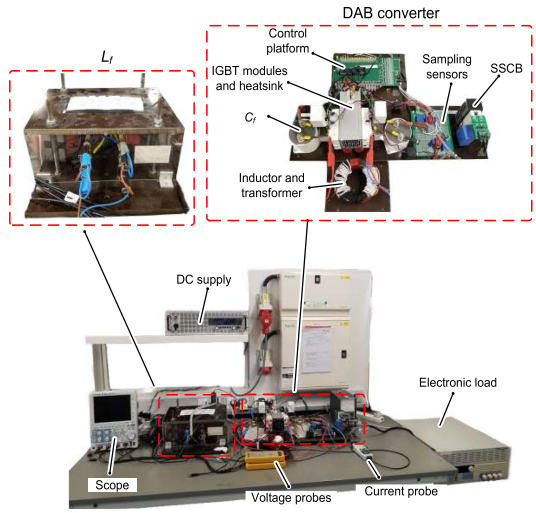

Fig. 18. Experiment setup.

TABLE V
HARDWARE COMPONENTS

Component	Description	Parameters
Switching devices	SKM75GB128D	V_{CES}=1200V; I_c=100A
Pri/Sec capacitors	C4DEFPQ6380A8TK, Polypropylene	380uF; 400V
Magnetic components	MnZn Ferrites; 3.9mm^2 litz wire	L_m=3mH; L_p=0.3mH
Voltage sensors	LV 25-P	t_r=40us
Current sensors	LA 55-p	BW(-1dB) 200kHz

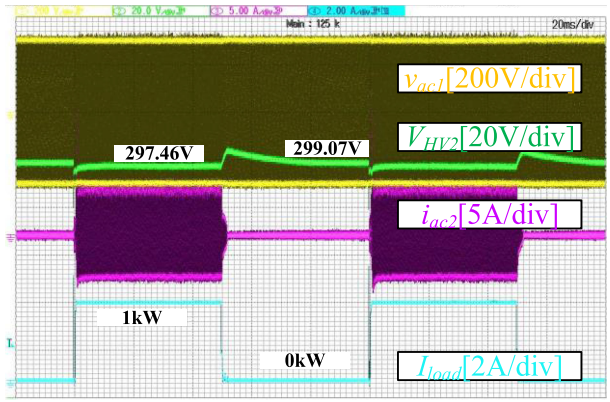

Fig. 19. MDCS-MPC-controlled DAB loaded with load variations @20 Hz. Prediction compensation disabled. $V_{HV1} = 300$ V. $V_{HV2\_ref} = 300$ V.

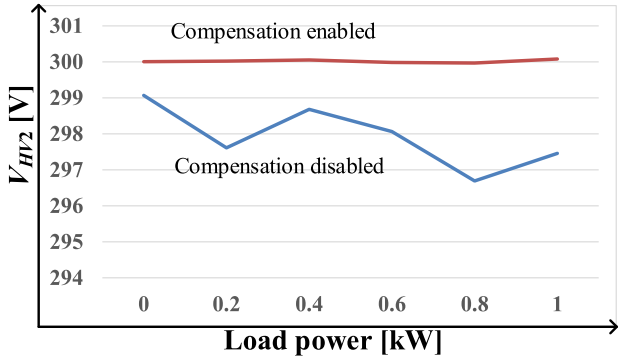

Fig. 20. Compensation for the prediction error as illustrated in Fig. 16. Operation under $V_{HV1} = 300$ V and $V_{HV2\_ref} = 300$ V over the whole power range.

OFF by a solid-state circuit breaker. Bench power supply EA-PS 9360-40 3U (1 Output, 0–360 V, 0–40 A) is connected directly to the DAB providing stiff input voltage V_{HV1}. The experiment prototype is shown in Fig. 18. A TMS320F2837xD evaluation board from Texas Instruments has been adopted as the digital control platform that communicates with a host computer. IGBT device SKM75GB128D is used as full-bridge switches with 1.6 μs software dead time. Two 380 μF 400 V polypropylene capacitors from KEMET are utilized for each dc terminal. The integrated transformer and inductor ($Lp = 300$ μH) are made by MnZn ferrites with 3.9 mm^2 litzs wire. The magnetizing inductance is $L_m = 3$ mH. Circuit and control parameters in Table IV are used in the experiment, otherwise specified. The main components used in the prototype are summarized in Table V.

A. Steady-State Error Compensation of MDCS-MPC

The effectiveness of the steady-state error compensation loop proposed in Fig. 16 is verified in this section. Experiments are carried out under the condition: 300 V input voltage V_{HV1}, and 300 V output voltage reference V_{HV2_ref}. Waveforms of the MDCS-MPC without the compensation are captured in presence of load variation @20 Hz, as in Fig. 19. Except for the existence of the steady-state error, without compensation, the proposed MDCS-MPC demonstrates superior load disturbance rejection ability in the experiment. There is no oscillation in both transition and steady state. It is clear that there is a difference between the steady-state values when changing the load power. When the compensation loop is enabled, the steady error can be much smaller compared with the results without compensations. Fig. 20 shows the steady-state measurement results of the output voltage mean value.

B. Performance Comparisons

The experiment results with load step up/down are provided in Figs. 21 and 22. In Fig. 21, the input voltage is set at 300 V, output voltage reference is set at 300 V. The load power jumps between 1 kW and 210 W at a frequency of 20 Hz. In Fig. 22, the input voltage is reduced to 260 V. When compared with Fig. 21, the performance of TPS-DAB is deteriorated with PI controller. This confirms the assessment in Fig. 13. In contrast, when MDCS-MPC is used, the performance remains well even when the terminal voltage is changed. The MDCS-MPC has good performance throughout the voltage and power range. The steady-state waveforms of Figs. 21 and 22 are presented in Figs. 23 and 24, respectively.

Experiments on the step change of the reference voltage are also conducted. The output voltage references are changed

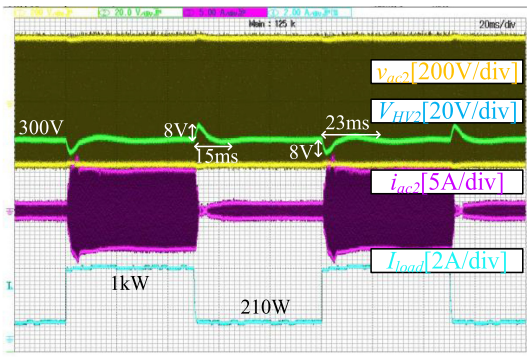

(a)

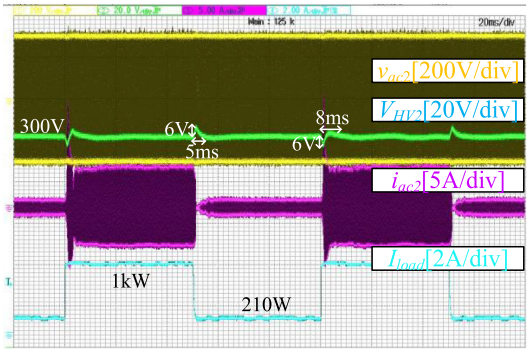

(b)

Fig. 21. Transition waveforms under $V_{HV1} = 300$ V and $V_{HV2\_ref} = 300$ V. (a) PI controller. (b) MDCS-MPC.

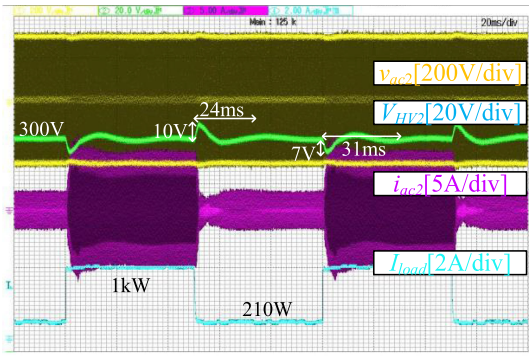

(a)

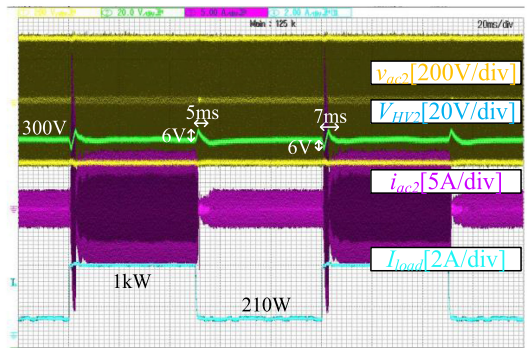

(b)

Fig. 22. Transition waveforms under $V_{HV1} = 260$ V and $V_{HV2\_ref} = 300$ V. (a) PI controller. (b) MDCS-MPC.

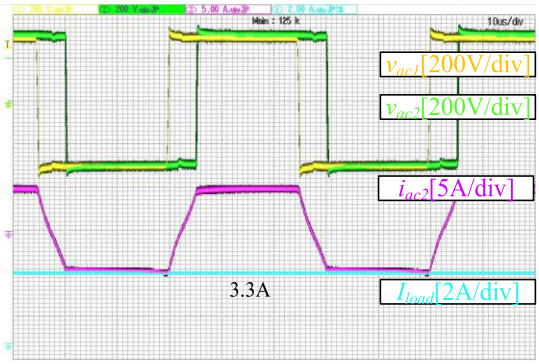

(a)

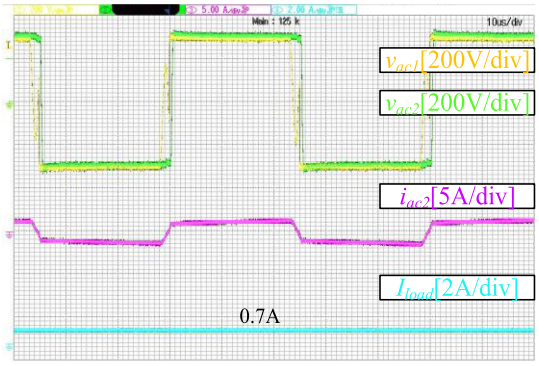

(b)

Fig. 23. Steady-state waveform under 300 V/300 V. (a) 1 kW. (b) 210 W.

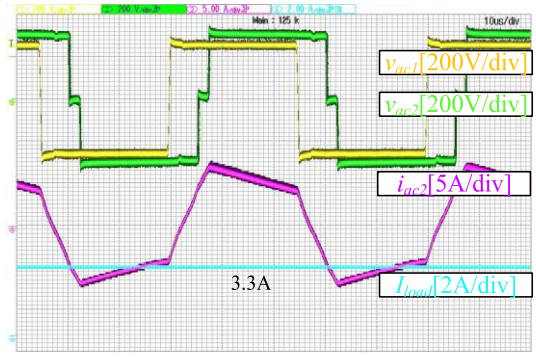

(a)

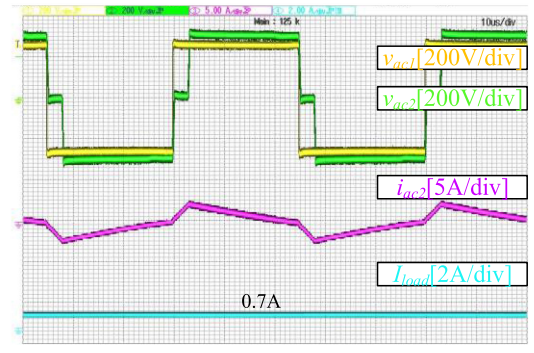

(b)

Fig. 24. Steady-state waveform under 260 V/300 V. (a) 1 kW. (b) 210 W.

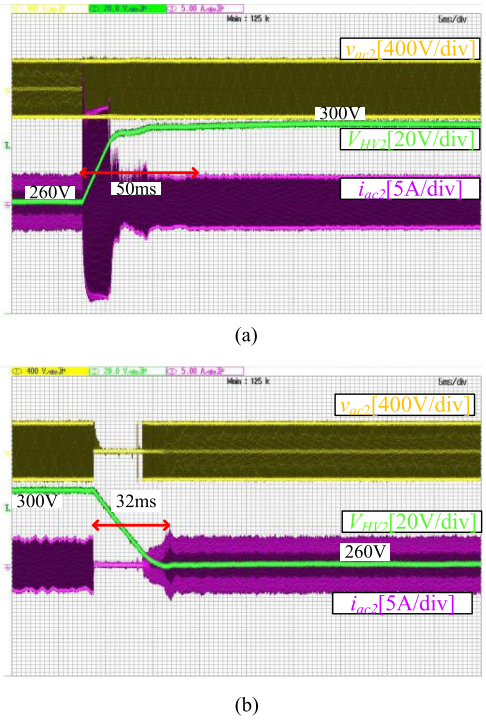

Fig. 25. Change of voltage reference V_{HV2_ref} with MDCS-MPC. (a) From 260 to 300 V. (b) From 300 to 260 V.

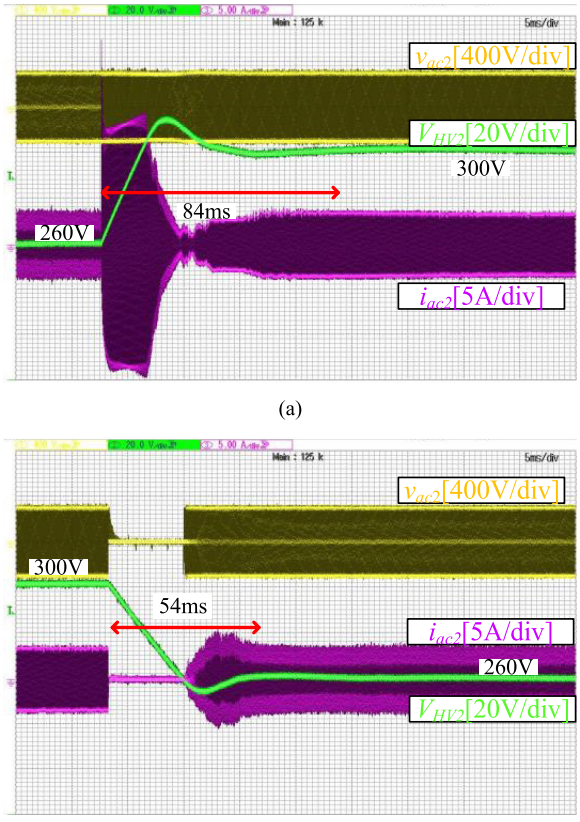

Fig. 26. Change of voltage reference V_{HV2_ref} with PI controller. (a) From 260 to 300 V. (b) From 300 to 260 V.

between 260 and 300 V. The transition results are presented in Figs. 25 and 26. In the experiment with MDCS-MPC, the voltage overshoot/dig is very small, thus ending in fast voltage tracking compared with the PI controller. The results again confirm the superior performance of the proposed MDCS-MPC in the regulation over the voltage reference.

C. Multiobjective Control

Another advantage of the proposed MDCS-MPC is the multiobjective control capability. The experiment circuit is configured as Fig. 15 to demonstrate the performance. The DAB converter is responsible for both output voltage regulation and input voltage stabilization. The cost function proposed in (19) is used. The value of L_f is 11 mH. The output capacitor C_{HV2} is reduced to 150 μF. The experiment result is shown in Fig. 27. The converter starts operating with G_3 disabled. The input voltage V_{HV1} oscillates due to the impedance instability [34]. The output voltage V_{HV2} is not affected. It is still tightly regulated at 270 V. At the time instance t_1, the stabilization term G_3 is enabled. The input voltage gets quickly stabilized. During the period t_1–t_2, the regulation of V_{HV2} is inevitably affected; however, both control objectives have been coordinately achieved at t_2.

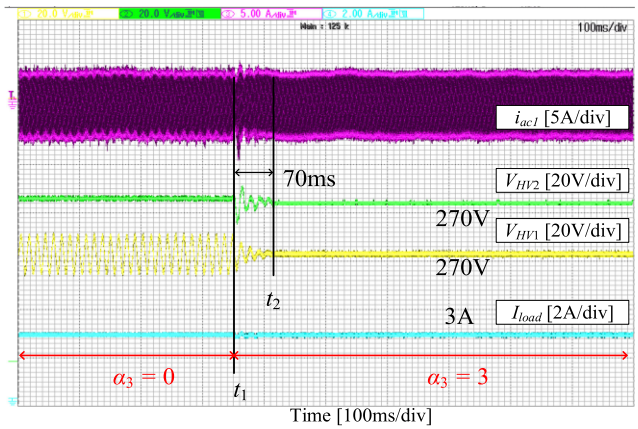

Fig. 27. Multiobjective control on both terminal voltages.

D. Computational Time

The computational time of the proposed MDCS-MPC is evaluated, as shown in Fig. 28. The PI controller takes 4.2 μs to run while, in contrast, the time to run MDCS-MPC varies with μ. In the experiment, $\mu = 11$ has already demonstrated good performance against PI controller, and it only takes 18.6 μs. Since 20 kHz switching frequency is utilized, 50 μs is available in one sampling period. Therefore, there is sufficient headroom for implementing A/D sampling, digital filters, MODBUS communication, protections, etc.

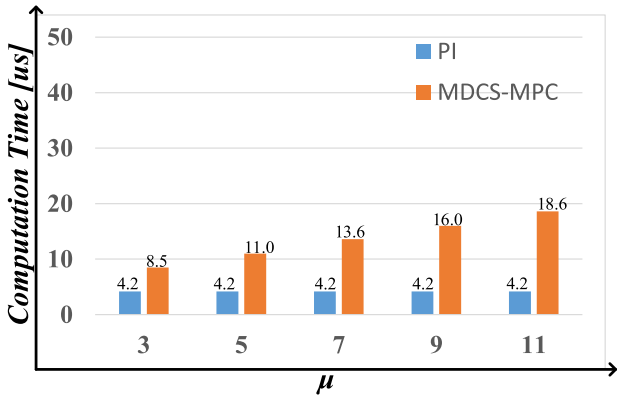

Fig. 28. Measurement of computational time.

VI. Conclusion

In this article, an MDCS-MPC is proposed to TPS-DAB. Compared with conventional PI control, MDCS-MPC provides benefits that are as follows.

1) The MDCS-MPC presents good performance throughout wide voltage and power range. It utilizes global control parameters, which eases the design.
2) The flexibility of the finite-control set-model-predictive control has been enabled by MDCS-MPC in TPS-DAB. Multiobjective control can be easily achieved.
3) It is feasible to implement the MDCS-MPC on commercial control platforms due to the use of a small prediction horizon.

The performance of the proposed MDCS-MPC and PI is compared in the experiment with TPS-DAB. Theoretical claims have been confirmed.

References

[1] K. W. Hu and C. M. Liaw, "Incorporated operation control of DC microgrid and electric vehicle," *IEEE Trans. Ind. Electron.*, vol. 63, no. 1, pp. 202–215, Jan. 2016.

[2] X. Zhaoxia, Z. Tianli, L. Huaimin, J. M. Guerrero, C.-L. Su, and J. C. Vasquez, "Coordinated control of a hybrid-electric-ferry shipboard microgrid," *IEEE Trans. Transp. Electrif.*, vol. 5, no. 3, pp. 828–839, Jul. 2019.

[3] S. Guenter *et al.*, "Load control for the DC electrical power distribution system of the more electric aircraft," *IEEE Trans. Power Electron.*, vol. 34, no. 4, pp. 3937–3947, Apr. 2019.

[4] L. Chen, L. Tarisciotti, A. Costabeber, F. Gao, P. Wheeler, and P. Zanchetta, "Advanced modulations for a current-fed isolated DC-DC converter with wide voltage operating ranges," *IEEE J. Emerg. Sel. Top. Power Electron.*, vol. 7, no. 4, pp. 2540–2552, Dec. 2019.

[5] Y. Shi, R. Li, Y. Xue, and H. Li, "Optimized operation of current-fed dual-active bridge DC-DC converter for PV applications," *IEEE Trans. Ind. Electron.*, vol. 62, no. 11, pp. 6986–6995, Nov. 2015.

[6] Y. W. Cho, W. J. Cha, J. M. Kwon, and B. H. Kwon, "High-efficiency bidirectional DAB inverter using a novel hybrid modulation for stand-alone power generating system with low input voltage," *IEEE Trans. Power Electron.*, vol. 31, no. 6, pp. 4138–4147, Jun. 2016.

[7] Q. Ye, R. Mo, and H. Li, "Stability analysis and improvement of a dual-active bridge (DAB) converter enabled DC microgrid based on a reduced-order low frequency model," in *Proc. IEEE Energy Convers. Congr. Expo.*, 2016, pp. 1–7.

[8] Q. Ye, Ran Mo, and H. Li, "Impedance modeling and verification of a dual-active bridge (DAB) DC/DC converter enabled DC microgrid in FREEDM system," in *Proc. IEEE 8th Int. Power Electron. Motion Control Conf.*, 2016, pp. 2875–2879.

[9] A. R. Alonso, J. Sebastian, D. G. Lamar, M. M. Hernando, and A. Vazquez, "An overall study of a dual-active bridge for bidirectional DC/DC conversion," in *Proc. IEEE Energy Convers. Congr. Expo.*, 2010, pp. 1129–1135.

[10] H. Bai, C. C. Mi, and S. Gargies, "The short-time-scale transient processes in high-voltage and high-power isolated bidirectional DC-DC converters," *IEEE Trans. Power Electron.*, vol. 23, no. 6, pp. 2648–2656, Nov. 2008.

[11] C. Mi, H. Bai, C. Wang, and S. Gargies, "Operation, design and control of dual H-bridge-based isolated bidirectional DC-DC converter," *IET Power Electron.*, vol. 1, no. 4, pp. 507–517, Dec. 2008.

[12] B. Farhangi and H. A. Toliyat, "Piecewise linear model for snubberless dual-active bridge commutation," *IEEE Trans. Ind. Appl.*, vol. 51, no. 5, pp. 4072–4078, Sep. 2015.

[13] S. Shao, H. Chen, X. Wu, J. Zhang, and K. Sheng, "Circulating current and ZVS-on of a dual-active bridge DC-DC converter: A review," *IEEE Access*, vol. 7, pp. 50561–50572, 2019.

[14] B. Zhao, Q. Yu, and W. Sun, "Extended-phase-shift control of isolated bidirectional DC-DC converter for power distribution in microgrid," *IEEE Trans. Power Electron.*, vol. 27, no. 11, pp. 4667–4680, Nov. 2012.

[15] B. Zhao, Q. Song, and W. Liu, "Efficiency characterization and optimization of isolated bidirectional DC-DC converter based on dual-phase-shift control for DC distribution application," *IEEE Trans. Power Electron.*, vol. 28, no. 4, pp. 1711–1727, Apr. 2013.

[16] S. Shao, M. Jiang, W. Ye, Y. Li, J. Zhang, and K. Sheng, "Optimal phase shift control to minimize reactive power for a dual-active bridge DC-DC converter," *IEEE Trans. Power Electron.*, vol. 34, no. 10, pp. 10193–10205, Oct. 2019.

[17] P. Karamanakos, T. Geyer, and S. Manias, "Direct voltage control of DC–DC boost converters using enumeration-based model-predictive control," *IEEE Trans. Power Electron.*, vol. 29, no. 2, pp. 968–978, Feb. 2014.

[18] B. Wang, V. R. K. Kanamarlapudi, L. Xian, X. Peng, K. T. Tan, and P. L. So, "model-predictive voltage control for single-inductor multiple-output DC–DC converter with reduced cross regulation," *IEEE Trans. Ind. Electron.*, vol. 63, no. 7, pp. 4187–4197, Jul. 2016.

[19] F. M. Oettmeier, J. Neely, S. Pekarek, R. DeCarlo, and K. Uthaichana, "MPC of switching in a boost converter using a hybrid state model with a sliding mode observer," *IEEE Trans. Ind. Electron.*, vol. 56, no. 9, pp. 3453–3466, Sep. 2009.

[20] S. Dutta, S. Hazra, and S. Bhattacharya, "A digital predictive current-mode controller for a single-phase high-frequency transformer-isolated dual-active bridge DC-to-DC converter," *IEEE Trans. Ind. Electron.*, vol. 63, no. 9, pp. 5943–5952, Sep. 2016.

[21] Z. Shan, J. Jatskevich, H. H.-C. C. Iu, and T. Fernando, "Simplified load-feedforward control design for dual-active-bridge converters with current-mode modulation," *IEEE J. Emerg. Sel. Top. Power Electron.*, vol. 6, no. 4, pp. 2073–2085, Dec. 2018.

[22] J. Huang, Y. Wang, Z. Li, and W. Lei, "Unified triple-phase-shift control to minimize current stress and achieve full soft-switching of isolated bidirectional DC-DC converter," *IEEE Trans. Ind. Electron.*, vol. 63, no. 7, pp. 4169–4179, Jul. 2016.

[23] K. Wu, C. W. de Silva, and W. G. Dunford, "Stability analysis of isolated bidirectional dual-active full-bridge DC–DC converter with triple-phase-shift control," *IEEE Trans. Power Electron.*, vol. 27, no. 4, pp. 2007–2017, Apr. 2012.

[24] T. Dragicevic, "model-predictive control of power converters for robust and fast operation of AC microgrids," *IEEE Trans. Power Electron.*, vol. 33, no. 7, pp. 6304–6317, Jul. 2018.

[25] L. Tarisciotti *et al.*, "model-predictive control for shunt active filters with fixed switching frequency," *IEEE Trans. Ind. Appl.*, vol. 53, no. 1, pp. 296–304, Jan. 2017.

[26] L. Tarisciotti, P. Zanchetta, A. Watson, S. Bifaretti, and J. C. Clare, "Modulated model-predictive control for a seven-level cascaded h-bridge back-to-back converter," *IEEE Trans. Ind. Electron.*, vol. 61, no. 10, pp. 5375–5383, Oct. 2014.

[27] T. Dragicevic, "Dynamic stabilization of DC microgrids with predictive control of point of load converters," *IEEE Trans. Power Electron.*, vol. 33, no. 12, pp. 10872–10884, Dec. 2018.

[28] N. Hou, W. Song, and M. Wu, "Minimum-current-stress scheme of dual-active bridge DC-DC converter with unified phase-shift control," *IEEE Trans. Power Electron.*, vol. 31, no. 12, pp. 8552–8561, Dec. 2016.

[29] A. Tong, L. Hang, G. Li, X. Jiang, and S. Gao, "Modeling and analysis of a dual-active-bridge-isolated bidirectional DC/DC converter to minimize RMS current with whole operating range," *IEEE Trans. Power Electron.*, vol. 33, no. 6, pp. 5302–5316, Jun. 2018.

[30] K. Zhang, Z. Shan, and J. Jatskevich, "Large- and small-signal average-value modeling of dual-active-bridge DC–DC converter considering power losses," *IEEE Trans. Power Electron.*, vol. 32, no. 3, pp. 1964–1974, Mar. 2017.
[31] S. Kouro, P. Cortés, R. Vargas, U. Ammann, and J. Rodríguez, "model-predictive control—A simple and powerful method to control power converters," *IEEE Trans. Ind. Electron.*, vol. 56, no. 6, pp. 1826–1838, Jun. 2009.
[32] J. Slotine and W. Li, *Applied Nonlinear Control*, vol. 199. Englewood Cliffs, NJ, USA: Prentice-Hall, 1991.
[33] P. Liutanakul, A.-B. Awan, S. Pierfederici, B. Nahid-Mobarakeh, and F. Meibody-Tabar, "Linear stabilization of a DC bus supplying a constant power load: A general design approach," *IEEE Trans. Power Electron.*, vol. 25, no. 2, pp. 475–488, Feb. 2010.
[34] J. Sun, "Impedance-based stability criterion for grid-connected inverters," *IEEE Trans. Power Electron.*, vol. 26, no. 11, pp. 3075–3078, Nov. 2011.
[35] T. Dragicevic, "Dynamic stabilization of DC microgrids with predictive control of point-of-load converters," *IEEE Trans. Power Electron.*, vol. 33, no. 12, pp. 10872–10884, Dec. 2018.

Linglin Chen received the M.Sc. degree in electrical engineering from Zhejiang University, Hangzhou, China, in 2016. He is currently working toward the Ph.D. degree with the Power Electronics, Machine and Control group at the University of Nottingham, Nottingham, U.K.

He was a Visiting Scholar with the Department of Energy Technology, Aalborg University, Aalborg, Denmark.

His current research interests include high-power ac/dc converters, high-current dc/dc power converters, model-predictive control, and power distribution system in more electric aircrafts.

Lyuyi Lin received the B.S. degree in electrical engineering from Tongji University, Shanghai, China, in 2016. She is currently working toward the Ph.D. degree in electrical engineering with Zhejiang University, Hangzhou, China.

Her current research interests include differential power processing in photovoltaic applications and digital control of power converters.

Shuai Shao (Member, IEEE) received the B.S. degree from Zhejiang University, Hangzhou, China, in 2010, and the Ph.D. degree in electrical and electronic engineering from the University of Nottingham, Nottingham, U.K., in 2015.

In 2015, he joined the College of Electrical Engineering, Zhejiang University, as a Lecturer. He has authored or coauthored more than 30 peer-reviewed technical papers. His research interests include solid-state transformers, bidirectional dc–dc converters, and fault detection in power converters.

Dr. Shao serves as a Guest Associated Editor for the IEEE JOURNAL OF EMERGING AND SELECTED TOPICS IN POWER ELECTRONICS.

Fei Gao (Member, IEEE) received the Ph.D. degree in electrical engineering from the University of Nottingham, Nottingham, U.K., in 2016.

From 2016 to 2019, he was with the Department of Engineering Science, University of Oxford, U.K., as a Postdoctoral Researcher. From 2010 to 2012, he was with Jiangsu Electric Power Research Institute, Nanjing, State Grid Corporation of China. Since 2019, he has been with Shanghai Jiao Tong University, Shanghai, China, as an Associate Professor. His current research interests include modeling, control, power management, and stability of power electronics-enabled microgrids and more electric transportation systems.

Dr. Gao was a recipient of the European Union Clean Sky Best Ph.D. Award in 2017 and IET Control and Automation Runner-Up Ph.D. Award in 2018.

Zhenyu Wang (Member, IEEE) received the B.S. degree in electrical engineering from Chongqing University, Chongqing, China, in 2012, and the M.S. and Ph.D. degrees in power electronics from the University of Nottingham, Nottingham, U.K., in 2014 and 2018, respectively.

He was a Visiting Scholar with the LEMUR Research Group at the University of Oviedo, Spain, from 2016 to 2017. He is currently a Research Fellow with the Power Electronics, Machines and Control Group, University of Nottingham, Nottingham, U.K. His research interests include SiC and GaN devices and applications, dc–dc converters for marine and aerospace applications, magnetic components for power electronic converters, and power converter control.

Patrick W. Wheeler (Senior Member, IEEE) received the B.Eng. (hons.) degree and the Ph.D. degree in electrical engineering for his work on matrix converters from the University of Bristol, Bristol, U.K., in 1990 and 1994, respectively.

In 1993, he moved to the University of Nottingham and worked as a Research Assistant with the Department of Electrical and Electronic Engineering. In 1996, he became a Lecturer in the Power Electronics, Machines and Control Group at the University of Nottingham. Since 2008, he has been a Full Professor in the same research group. He is currently the Head of the Department of Electrical and Electronic Engineering at the University of Nottingham and the Li Dak Sum Chair Professor in electrical and aerospace engineering with the University of Nottingham China, Ningbo, China. He has authored/coauthored 500 academic publications in leading international conferences and journals.

Prof. Wheeler is a member of the IEEE POWER ELECTRONICS SOCIETY AdCom and was an IEEE POWER ELECTRONICS SOCIETY Distinguished Lecturer from 2013 to 2017.

Tomislav Dragičević (Senior Member, IEEE) received the M.Sc. and industrial Ph.D. degrees in electrical engineering from the Faculty of Electrical Engineering, Zagreb, Croatia, in 2009 and 2013, respectively.

From 2013 to 2016, he was a Postdoctoral Research Associate with Aalborg University, Denmark. Since 2016, he has been an Associate Professor with Aalborg University, where he leads an Advanced Control Laboratory. He was a Guest Professor at Nottingham University, U.K., during spring/summer of 2018. His current research interests include design and control of microgrids, and application of advanced modeling and control concepts to power electronic systems. He has authored and coauthored more than 155 technical papers (more than 70 of them are published in international journals, mostly IEEE Transactions) in his domain of interest, eight book chapters, and a book in the field.

Dr. Dragičević serves as an Associate Editor for the IEEE TRANSACTIONS ON INDUSTRIAL ELECTRONICS, IEEE EMERGING AND SELECTED TOPICS IN POWER ELECTRONICS, and IEEE INDUSTRIAL ELECTRONICS MAGAZINE. He is a recipient of the Končar prize for the best industrial Ph.D. thesis in Croatia, and the Robert Mayer Energy Conservation Award.